


Effect of curing temperature on surface and subsurface properties of polyurethane elastomer

I.A. Morozov ¹ ✉, A.Yu. Beliaev¹, M.G. Scherban²

¹ Institute of Continuous Media Mechanics of the Ural Branch of Russian Academy of Science, Perm, Russia

² Perm State University, Perm, Russia

✉ ilya.morozov@gmail.com

Abstract. Polyurethane elastomers are a class of polymers with two-phase segmented structure. The study of their features at the microstructure level will make it possible to control both macroscopic physical and mechanical properties of polymers and functional properties of surfaces. Polyurethanes of the same formulation were synthesized in this work, varying the curing temperature from 30 to 90 °C. Atomic force microscopy, dynamic mechanical analysis, and wettability were used in the study. Stiff fibrillar supramolecular structures (elastic modulus 14–22 MPa), distributed in a softer matrix, are formed in the polymers. Phase inhomogeneities are hidden under the surface by a soft nanolayer of variable thickness. An increase in the curing temperature leads to an increase in the thickness of this layer, and the stiff structure transforms from homogeneous to a network of agglomerates. Wettability, free surface energy and macroscopic viscoelastic properties nonlinearly depend on the curing temperature, which is explained by the physical and mechanical properties of the stiff and soft phases.

Keywords: polyurethane; microstructure; atomic force microscopy; physical and mechanical properties

Acknowledgements. *The research was carried out at the expense of the grant of the Russian Science Foundation No. 23-22-00064.*

Citation: Morozov IA, Beliaev AY, Scherban MG. Effect of curing temperature on surface and subsurface properties of polyurethane elastomer. *Materials Physics and Mechanics*. 2023;51(6): 107-118. DOI: 10.18149/MPM.5162023_10.

Introduction

Polyurethane elastomers are segmented polymers consisting of soft and hard segments [1]. Primary hard segments form secondary supramolecular structures (fibrils, cylinders, ribbons, meshes, globules) in a softer matrix. The properties of such structures depend on the chemical composition [2–5], the curing time or temperature [6,7], the presence of filler particles in the composition [8–10], the thickness of the material [11], additional heat treatment [12,13], the history of mechanical loading [14,15]. It has been established that the heterogeneous structure of polyurethane is covered with a low-molecular-weight nanolayer of the soft phase [16,17]. The images for the phase separation of polyurethane, presented in the majority of the studies, were obtained using the tapping mode of atomic force microscopy (AFM), and are in fact images of some transitional near-surface region [17,18].

In addition to obtaining materials with a given set of structural properties, a promising modern direction is modification of the polyurethane surface. In the latter case, this refers to improving specific functional characteristics: biocompatibility [19–22], antibacterial properties

[23], wettability [24], gas permeability [25]. The best results can be achieved by taking into account both the presence of a surface nanolayer and the particulars of phase separation in the internal supramolecular structure. In particular, it has been established that plasma ions interact differently with soft and hard subsurface regions; in some cases, this significantly increases the crack resistance and deformability of coatings with improved biocompatibility [21,22].

To date, numerous works have focused on the physical and mechanical characteristics of polyurethane elastomers. However, the results obtained on the structural characteristics of elastomers are often interpreted based on indirect data (typically, spectroscopic studies). This is insufficient given the complex structure of polyurethanes. Thus, study of the surface and subsurface properties of phase-separated polyurethanes is important both for predicting the physical and mechanical properties of materials and for their directed functionalization at the structural level of the material.

This paper considers polyurethanes with the same composition but synthesized with different curing temperatures. We focused on the microstructural surface and subsurface properties of polymers and on the characteristics of their phase separation. Supramolecular structures with different structural and physico-mechanical properties depending on the curing temperature were obtained in the materials, affecting the macroscopic characteristics of the materials.

Materials and Methods

Production of materials. Polyurethanes were prepared from commercially available prepolymer (urethane prepolymer based on polyester and toluene diisocyanate) and crosslinking agent (13.2 % MOCA hardener, 84.7 % polyfurite plasticizer, 2.1 % voranol catalyst) in a mass ratio of 100:47. The components were heated at 80 °C and evacuated. The mixture was vacuum-dried for 24 hours as plates with a free upper surface 2 mm thick. The curing temperature T was set to 30, 50, 70 or 90 °C. The resulting specimens are marked T30, T50, T70 and T90. The polyurethane does not fully cure in 24 hours at a low temperature. For this reason, the mixtures T30 and T50 were further cured after 24 hours at $T = 70$ °C for another 24 hours.

Wettability and free energy of the surface. The wetting contact angle was determined using a goniometer by the sessile drop method. Water and diethylene glycol were used as test liquids; droplet sizes ranged from 2 to 3 mm. The free surface energy was calculated by the Owens–Wendt–Rabel–Kaelble method as the sum of the dispersion (energy of Van der Waals interactions) and polar (dipole interactions and energy of hydrogen bonds) components.

Dynamic mechanical analysis. Rectangular specimens were tested for uniaxial tension on a DMA/SDTA861e Dynamic Mechanical Analyzer (METTLER TOLEDO, Switzerland). The base of the specimen is 10 mm long, about 6 mm wide, about 2 mm thick. The tests were carried out at a temperature of 25 °C and a deformation amplitude of 3 %, varying the frequency from 0.5 to 50.5 Hz in 5 Hz increments.

Atomic force microscopy. An AFM Ntegra Prima in nanomechanical mapping mode was used. ScanAsyst-Air probes with calibrated tip radii $R \sim 3\text{--}5$ nm and bending stiffness of the beam $k \sim 0.4\text{--}0.5$ nN/nm were used. In this mode, the probe indents the selected area at a high speed (10 nm/ms was set; the indentation frequency was ~ 20 Hz taking into account the vertical displacement of the piezoelectric scanner at 350 nm). The high indentation speed allows obtaining high-resolution data in the specimen plane: an array of interaction curves $d(z)$ of the probe with the surface when the probe approaches the surface and withdraws from it, where d is the cantilever bending, z is the relative distance between the probe and the specimen; interaction force: $F = kd$.

The tip of the probe is strongly attracted to the surface under the action of van der Waals forces at some distance from the surface (point A in Fig. 1). The deviation d_c of the probe from the equilibrium position after the jump to contact has been completed is a measure of the Hamaker constant H_s of the surface [26]: $H_s = 9k^2d_c^6 / (R^2H_t)$, where H_t is the Hamaker constant of the probe material ($H_t = 18 \cdot 10^{-20}$ J for a probe made of silicon nitride). We assume that the indentation of the probe into the material begins at point B, then the indentation depth $u = (z - z_b) - (d - d_b)$. The polymer is indented in the segment BC until a given maximum load of ~ 3 nN is reached (the average indentation depth at such a load was 50 nm). The specimen is then unloaded as the probe is removed from the surface.

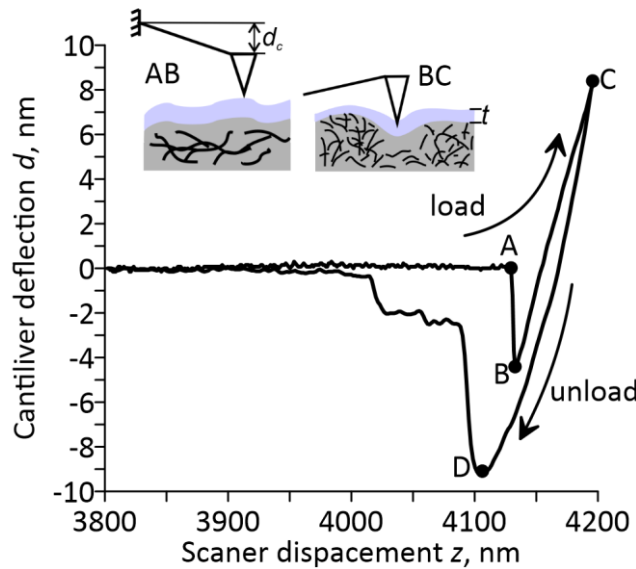


Fig. 1. Typical curve for interaction of AFM probe with polyurethane surface: loading and unloading curves, as well as characteristic stages of interaction are shown

The maximum magnitude of the force at the time when the probe separates from the surface (point D in Fig. 1) is related to the free energy of the surface and is widely used in the Derjaguin–Muller–Toporov or Johnson–Kendall–Roberts elastic indentation models to subsequently determine the elastic modulus of the surface. In general, the observed relief depends on the applied force: the probe pushes through the soft outer nanolayer with increasing loads, starting to detect the internal structures of the polymer hidden under the surface. The algorithms we developed [27] allow to monitor these changes in relief, as well as to estimate the thickness t of the upper homogeneous layer covering the subsurface structures.

The presence of a soft upper layer makes it difficult to use models for determining the elastic modulus taking into account the adhesion of the probe to the surface as a measure of the free energy of the surface. In this case, a comparative analysis of local stiffness is carried out using the Sneddon approach [28,29] for a parabolic indenter with non-uniform depth distribution of the elastic modulus: $E_i(u_i) = \frac{(1-\nu^2)}{4\sqrt{Ru_i}} \frac{d_i - d_{i-1}}{u_i - u_{i-1}} k$, where $\nu = 0.5$ is Poisson's ratio.

The polymer has inelastic properties, i.e., the loading and unloading curves do not coincide. We use the viscosity coefficient as a measure of the viscoelastic properties of the surface. Similar to the elastic modulus, it depends on the indentation depth [30,31]:

$\eta(u_i) = \frac{1}{du/dt} \frac{F_{dis}(1-\nu^2)}{6\sqrt{Ru_i}}$, where the dissipative component of the load F_{dis} is calculated as the difference between the forward and reverse scanning directions F_a and F_r : $F_{dis} = (F_a - F_r)/2$.

Results and Discussion

Let us start by considering some macroscopic properties of polymers. The material T30 has the best hydrophilic properties (Fig. 2); the wettability deteriorates with an increase in the curing temperature (the contact angle increases), and does not change significantly in the curing temperature range from 50 to 90 °C. The free energy of the surface behaves similarly (Fig. 2); its variation is due to a decrease in the polar component (the energy of hydrogen bonds and dipole interactions); the dispersion component increases slightly.

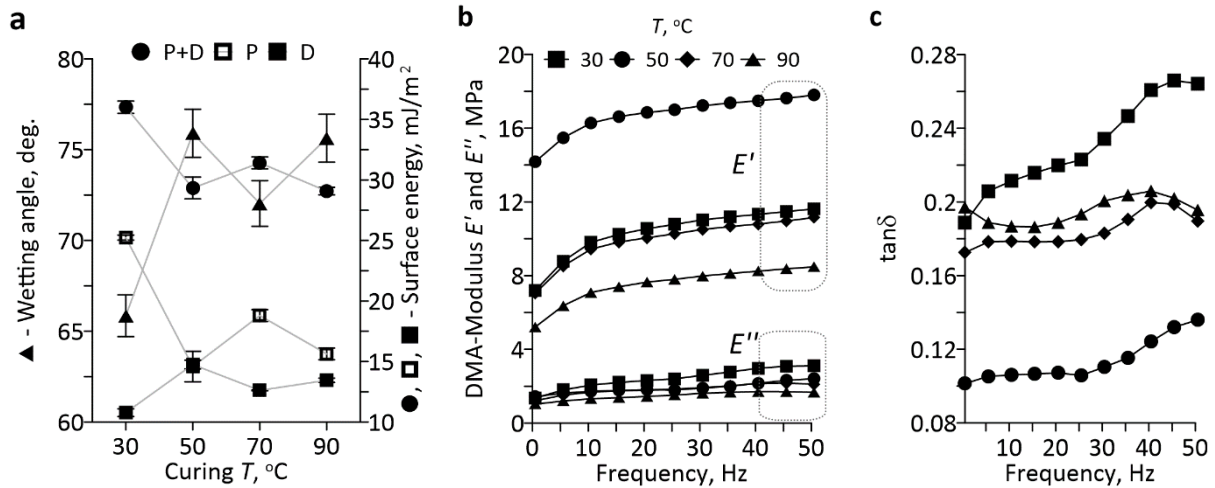


Fig. 2. Contact angle and free energy of the surface: dispersive (D) and polar components (P) (a), DMA-measurements: storage and loss moduli (b), tangent of mechanical losses (c)

DMA tests established (Fig. 2(b,c)) that the storage modulus E' of polyurethane T50 is approximately twice as high as those of other materials; the same polymer also has the least pronounced viscous characteristics. The material T90 turned out to be the softest from standpoint of DMA tests, T30 has the greatest mechanical losses.

The internal structure of synthesized polyurethanes (Fig. 3) represents rigid fibrillar structures (supramolecular formations with a high concentration of hard polyurethane segments), unevenly entangled in a softer matrix (regions of high concentration of soft segments and a small proportion of disordered hard segments). The most dense and homogeneous structure is produced at curing temperatures of 30–50 °C (Fig. 3(a,b)). In these cases, dense hard agglomerates are observed, the length of individual fibrils is no more than 20 nm. An increase in temperature leads to a more porous and more heterogeneous structure of hard segments in the form of a fibrillar mesh (Fig. 2(d)); the size of the fibrils can reach 1 μm or more. The mean fibril width is 3–5 nm, which corresponds to the size of perpendicularly packed primary hard segments of polyurethane [2].

Polyurethane surfaces were smooth and uniform (see the insets in Fig. 3). The fibrillar heterogeneities in polymers (see enlarged view in Fig. 3) are hidden under the surface by a nanolayer with variable thickness t , homogeneous in its mechanical characteristics. The thickness of this outer layer was estimated by the transformations in the relief structure during indentation: given a small force, the AFM probe first interacts with the outer layer, pushing through this layer with increasing load, as the internal structure gradually evolves.

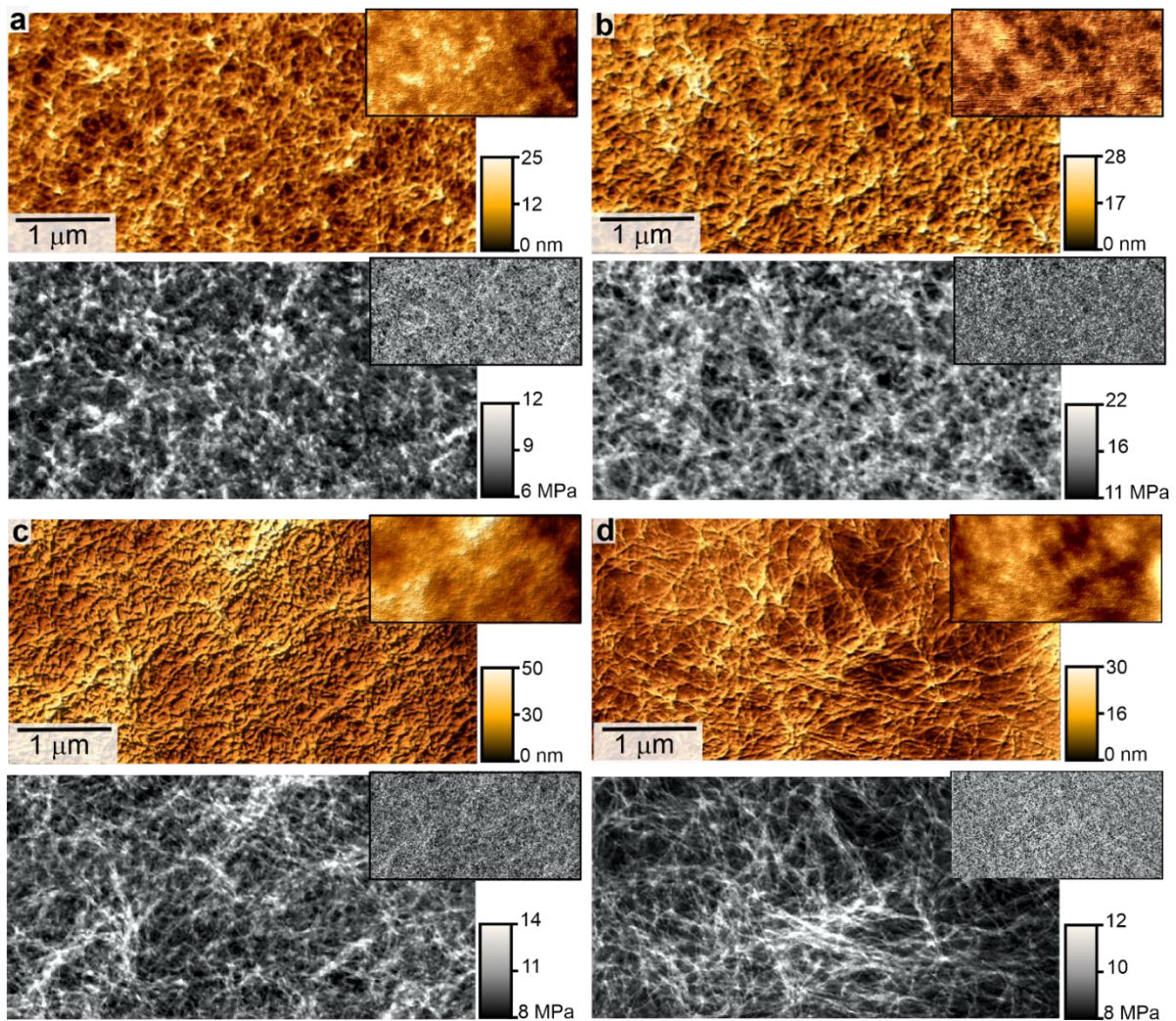


Fig. 3. AFM images for relief (top row) and stiffness maps (bottom row) of polyurethanes at curing temperatures of 30 (a), 50 (b), 70 (c) and 90 °C (d). Enlarged fragments of subsurface structures are shown; the corresponding surface maps are shown in the insets

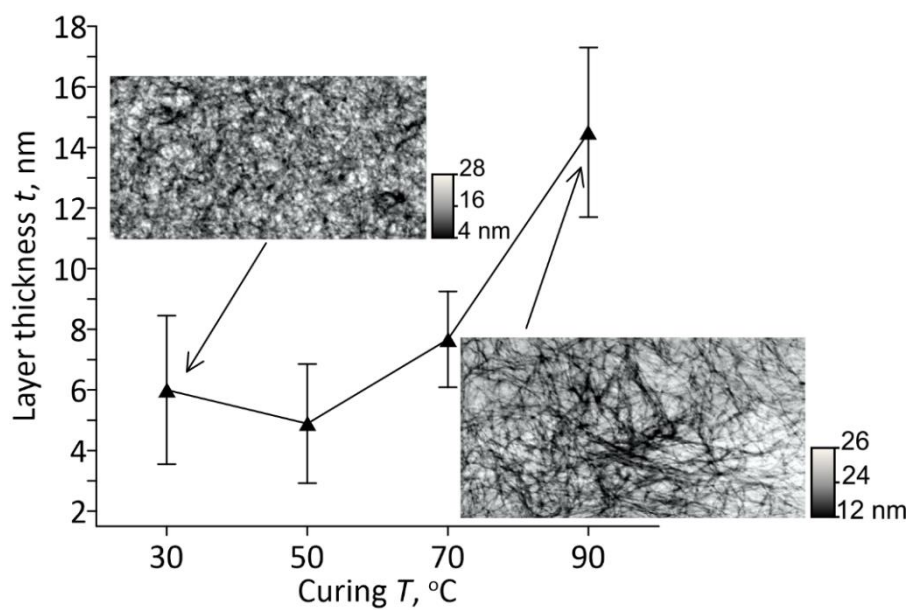


Fig. 4. Thickness of polyurethane surface nanolayer covering the elevations. The insets show the corresponding thickness distribution maps. AFM images of reliefs are shown in Fig. 3

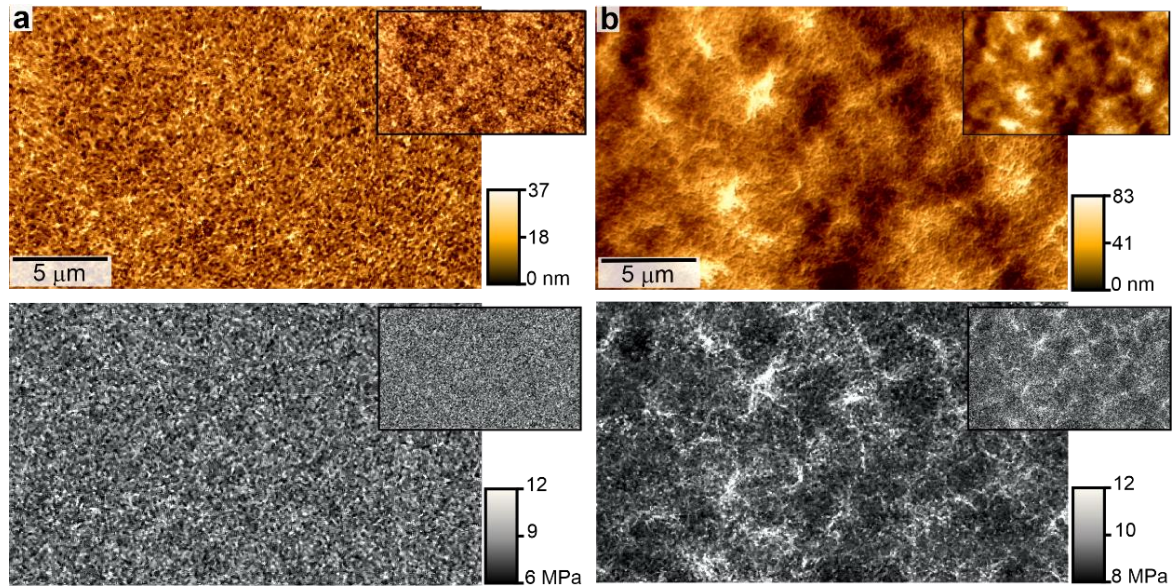


Fig. 5. Representative AFM images of relief and elastic modulus of subsurface (enlarged) and surfaces (insets) of materials T30 (a) and T90 (b)

The thickness of the outer layer (Fig. 4(a)) depends both on the features of the internal structure and on the curing temperature. The lowest thickness of the layer is achieved at elevations of subsurface relief, i.e., the peaks of hard supramolecular agglomerates (Fig. 4(b,c)); the thickness does not change at curing temperatures of 30–50 °C, then increasing from 5 to 14 nm. The thickness of the nanolayer in the regions free of hard subsurface structures (depressions of subsurface relief) does not change, fluctuating in the vicinity of 22–24 nm. In the latter case, the layer has no clear boundaries, merging into the matrix.

Representative AFM images are shown in Fig. 5: the reliefs for T30 and T50 (T50 is not shown here) are relatively flat. Agglomeration of hard structures occurs at curing temperatures of 70 and 90 °C (see the stiffness map in Fig. 5(b)); the size of the agglomerates is ~ 5 μm.

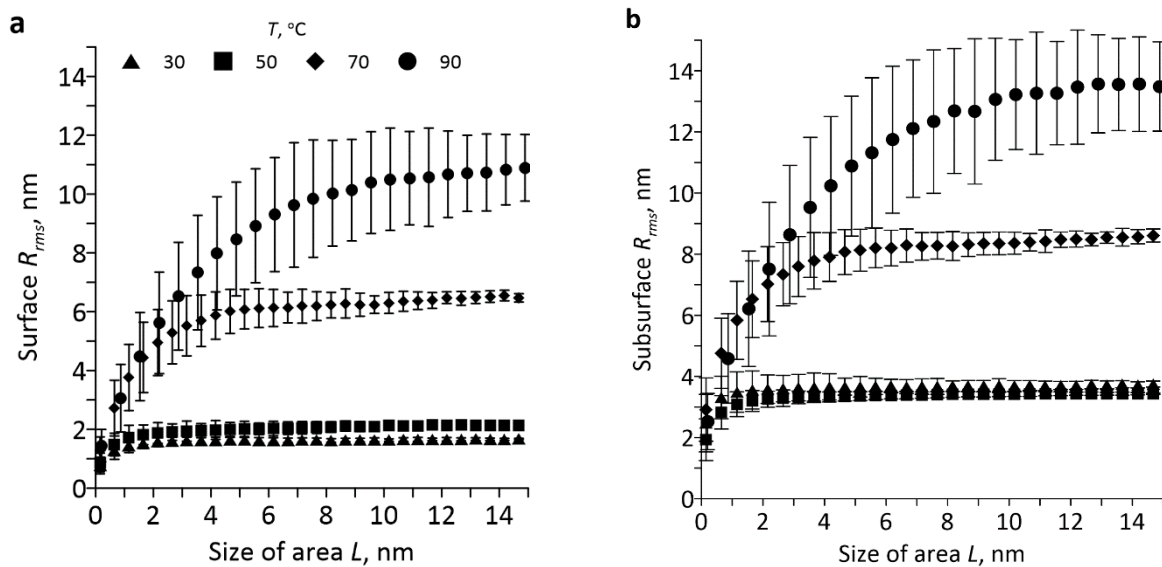


Fig. 6. RMS roughness of the surface (a) and subsurface reliefs (b) depending on the size of the region

Quantitative analysis of structural heterogeneities was performed by calculating the RMS roughness R_{rms} of the relief depending on the size L of a square region randomly selected in the image. The mean roughness increases, reaching the asymptote at a certain size L_{crit} of the region (Fig. 6). L_{crit} is the smallest size starting from which the distribution of hard structures in polyurethane can be considered homogeneous, in other words, the critical size of the heterogeneity: the size of the heterogeneity does not exceed $1.5\text{--}2\ \mu\text{m}$ $T < 50\ ^\circ\text{C}$, then sharply increasing to $13\ \mu\text{m}$ at $T = 90\ ^\circ\text{C}$.

Subsurface structures in AFM images are located at different heights relative to each other. What we actually observe is a fragment of a three-dimensional supramolecular structure of the material. We binarize representative AFM images of a three-dimensional subsurface relief, leaving only what lies within the mean height of the image $\pm 3\ \text{nm}$ (the mean fibril width). As a result, we obtain slices of the subsurface structure. The fractal dimension D of the obtained images is shown in Fig. 7 (to calculate D , we divide the image into squares with the side size L and calculate the number N of non-empty squares; we can prove that L and N are related by a fractal dependence: $N \sim L^{-D}$).

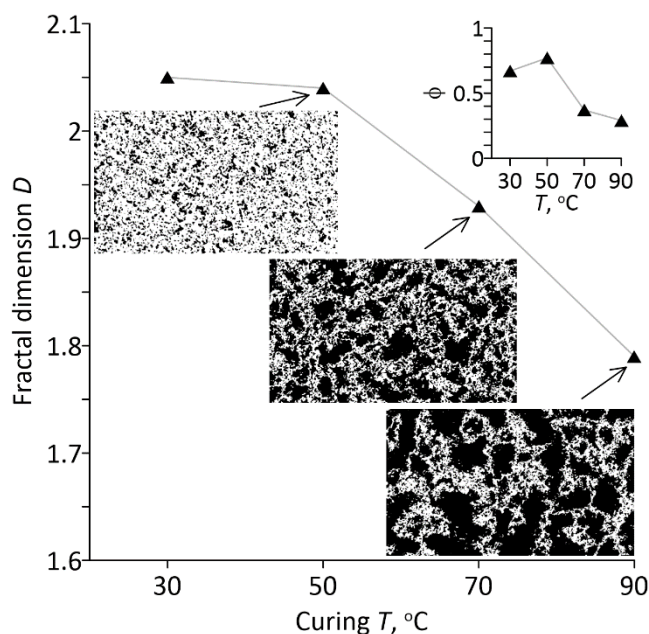


Fig. 7. Fractal dimension D and fraction of the mesh containing hard subsurface agglomerates. The insets show slices of the corresponding structures obtained by binarization of representative AFM images. The light regions correspond to hard subsurface structures.

The structure of the material T30 is close to that of T50 and is not shown

The fractal dimension of the mesh of hard structures is close to 2 for materials T30 and T50, which corresponds to a homogeneous (cluster-free) distribution of hard structures in these materials. The picture radically changes with an increase in the curing temperature: the rigid supramolecular structure in polyurethanes T70 and T90 is a mesh of fractal agglomerates, whose tortuosity and heterogeneity increase with the curing temperature. The observed agglomerates are tangled dense clumps of fibrillar structures. The fraction of the material forming a dense hard mesh decreases from 70–80 % (T30, T50) to 40–30 % (T70, T90); the densest structure is observed in the T50 material. The space between the agglomerates is filled with a sparse mesh of individual fibrils (see Fig. 3(d)).

The jump d_c of the probe to the surface (see Fig. 1) is proportional to the Hamaker constant. The measurements showed that the mean values of d_c (Fig. 8(a)) do not change significantly with an increase in the curing temperature. The Hamaker constant, in turn, is directly proportional to the dispersion component of the free energy (interatomic interactions based on van der Waals forces) of the surface [32]. This result is confirmed by the experiments conducted to measure the wettability and free energy of the surface (Fig. 2(a)): the change in the dispersion component of the surface free energy correlates with the d_c measurements.

Maps of the jump to the surface made by the probe (see the insets in Fig. 8(a)) are inhomogeneous, i.e., there are regions with high and low values with $\pm 10\%$ deviation from the mean (statistical distributions of d_c are close to normal). For example, regions with low values of d_c can be seen in the d_c map for T30 in the form of circular segments. The magnitude of the jump depends on the local irregularities in the relief [33]. In our case, the observed inhomogeneities in d_c are not related either to the outer surface of the polymer or to its internal fibrillar structure (see Fig. 3). This is to say that the outer nanolayer has region with inhomogeneous activity. No correlation was found between the curing temperature and the properties of these inhomogeneities.

The internal structure of the polymer does not affect the magnitude of the jump to the surface (the distance d_c+t between the probe and the subsurface is quite large). That is, the Hamaker constant calculated from d_c is a characteristic of only the outer layer. At the same time, as established below, the surface free energy measured by wetting depends on both the internal structure and the external nanolayer.

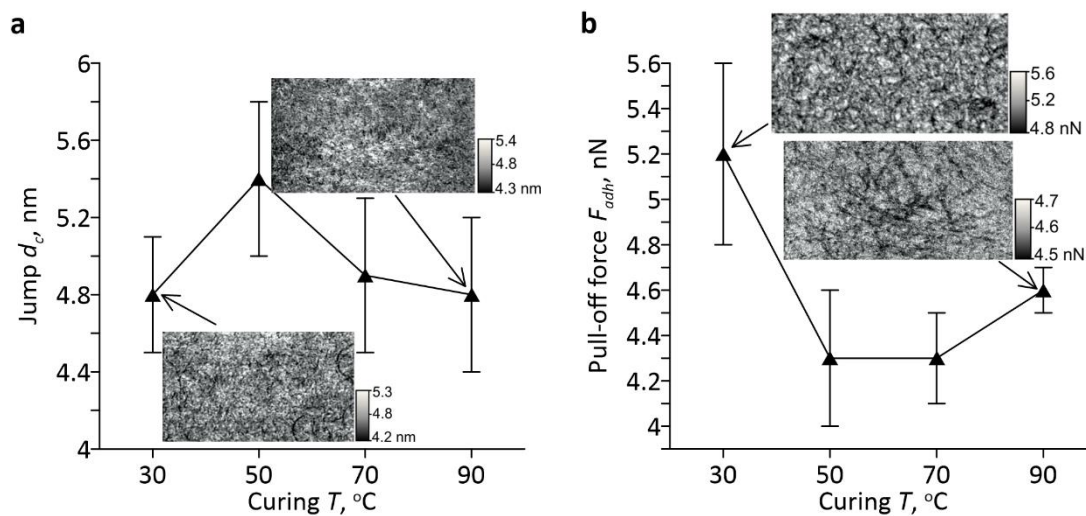


Fig. 8. Jump of the probe to the surface (a) and pull-off force (b). The insets show the corresponding maps. AFM images of reliefs are shown in Fig. 3

The force at the instant when the probe separates from the surface is traditionally associated with the surface free energy: it is maximum for the surface T30, reaches a minimum at T50–T70, and then begins to grow. These results (Fig. 8(b)) correlate with the changes in the surface free energy and the contact angle (Fig. 2(a)). Inhomogeneities in the maps characterizing the adhesion of the probe to the material (see the insets in Fig. 8(b)) are related to the internal structure of the polymer: regions with lower adhesion values correspond to hard structures in the elevations of subsurface relief; high adhesion values correspond to softer depressions. However, despite the pronounced inhomogeneities in the adhesion maps, the differences between the adhesion of hard and soft regions do not exceed $\pm 5\%$.

As the curing temperature increases, the thickness of the surface layer increases (see Fig. 4) and the adhesion inhomogeneities caused by subsurface structures become even less pronounced. On the other hand, the decrease in the surface free energy (Fig. 2(a)) occurs due to the polar component. Thus, the polar properties of hard subsurface structures influence the change in the polar component of the surface free energy.

The force experienced by the probe as it detaches from the material is used in common models for calculating Young's modulus of surfaces as a measure of the specific surface free energy. However, as shown above, the exact manner in which the measured adhesion is influenced by subsurface structures remains uncertain. This narrows the scope of application of the existing models, and the Sneddon approach was used in this paper to estimate the elastic modulus. The obtained maps of the elastic modulus are shown in Figs. 3 and 5. Figure 9(a) shows the mean values separately for hard (elevations in the subsurface relief) and soft (depressions) regions: with the exception of one of the polyurethanes, the modulus of hard subsurface structures does not change (14 MPa). The modulus of soft regions and the surface layer increases from 7 (T30) to 9 MPa (T90). That is, a part of the primary hard polyurethane segments does not have time to assemble into fibrillar structures at high curing temperatures, and remains distributed in the soft matrix. Polyurethane T50 does not follow this trend: the stiffness of its structures is 1.5 times higher than that of other materials.

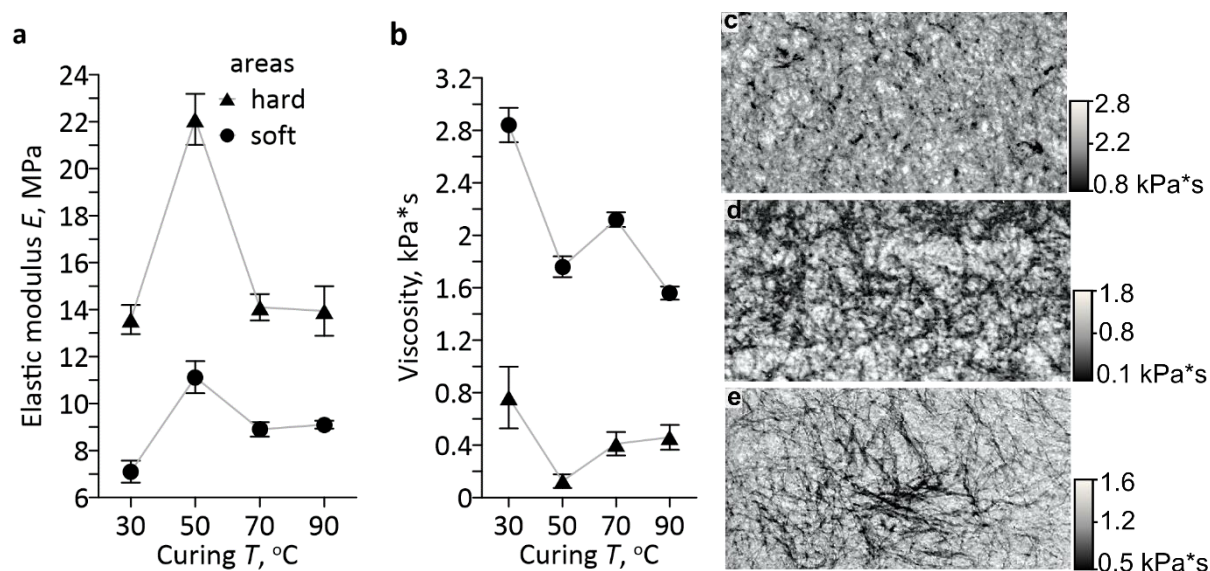


Fig. 9. Elastic modulus (a) and viscosity (b) of hard (elevations of subsurface relief) and soft segments of polyurethanes; viscosity distribution maps of materials T30 (c), T50 (d) and T90 (e). AFM images of reliefs are shown in Fig. 3

The viscosity (Fig. 9(b)) of hard subsurface structures is significantly lower than in the segments of the soft matrix. In general, the viscosity of the soft matrix decreases, which can be explained by an increase in the concentration of disordered primary hard polyurethane segments in it. Polyurethane T30 has the most pronounced viscous properties of both hard structures and the matrix. The low curing temperature of this material did not allow for it to produce a sufficient number of polymer crosslinks, giving elasticity to the polymer matrix.

Notably, both the elastic modulus and the viscosity measured using atomic force microscopy showed a good correlation with the moduli and tangent of mechanical losses obtained by DMA. The most elastic material is T50, and the strengthening of elastic properties occurs mainly due to a decrease in the viscosity of hard structures. The supramolecular hard

mesh in this material is the densest (see Fig. 7), therefore its viscoelastic properties have a significant impact on the macroscopic behavior of the material (see Fig. 2(b, c)).

Conclusion

We synthesized polyurethanes with a curing temperature from 30 to 90 °C. It was established that the materials form hard (elastic modulus of 14–22 MPa) subsurface supramolecular structures (nanofibrils and agglomerates) located in a softer matrix (elastic modulus of 7–9 MPa). The most dense and homogeneous hard subsurface structure is formed in polyurethanes with a curing temperature of 30–50 °C; the structure becomes heterogeneous and loose with a further increase in temperature: agglomerates up to several microns appear; the soft phase space between the agglomerates is crossed by a mesh of extended fibrils. This entire internal heterogeneous structure of polyurethanes is hidden by a soft surface nanolayer. The mean thickness of this layer depends on the curing temperature, increasing from 6 (30 °C) to 14 nm (90 °C).

The observed fibrils and their agglomerates are secondary supramolecular structures with a high concentration of primary hard segments. Polymerization and formation of chemical crosslinking between macromolecules consisting of primary hard and soft segments occur during the curing of polyurethane. The polymer changes from a viscous state to an elastic one. At the same time, hard supramolecular structures are formed in polyurethanes [1,6]. A possible explanation for the differences in the structure is that the rate of chemical crosslinking and formation of a continuous mesh of macromolecules increases under curing at high temperatures, which makes it difficult to form a large number of supramolecular structures.

The curing temperature affects not only the structural features of the phase separation, but also the physico-mechanical properties of polymers: a correlation is shown between the features of the activity of inhomogeneous surfaces at the structural level and macroscopic measurements of the wettability and free energy of the surface (decreases with increasing curing temperature).

Curing at low temperature produces homogeneous and hard materials with high surface energies and pronounced dissipative properties (polyurethane obtained at 50 °C was the most stiff and elastic; the one obtained at 90 °C was the least stiff). The viscosity of materials obtained at high temperature is lower, they are more elastic, and their structure is more heterogeneous. All these results are explained by the mechanical properties of the supramolecular structures of these materials. Studies into these processes provide the key to obtaining polymers with the required properties.

References

1. Petrović ZS, Ferguson J. Polyurethane elastomers. *Progress in Polymer Science*. 1991;16(5): 695–836.
2. Sheth JP, Klinedinst DB, Wilkes GL, Yilgor I, Yilgor E. Role of chain symmetry and hydrogen bonding in segmented copolymers with monodisperse hard segments. *Polymer*. 2005;46(18): 7317–7322.
3. Klinedinst DB, Yilgor I, Yilgor E, Zhang M, Wilkes GL. The effect of varying soft and hard segment length on the structure–property relationships of segmented polyurethanes based on a linear symmetric diisocyanate, 1,4-butanediol and PTMO soft segments. *Polymer*. 2012;53(23): 5358–5366.
4. Tocha E, Janik H, Debowski M, Vancso GJ. Morphology of polyurethanes revisited by complementary AFM and TEM. *Journal of Macromolecular Science, Part B*. 2002;41(4-6): 1291–1304.
5. Yilgor I, Yilgor E, Wilkes GL. Critical parameters in designing segmented polyurethanes and their effect on morphology and properties: A comprehensive review. *Polymer*. 2015;58: A1–A36.
6. Kimball ME, Fielding-Russell GS. Effect of cure temperature on urethane networks. *Polymer*. 1977;18(8): 777–780.
7. Cheng BX, Gao WC, Ren XM, Ouyang XY, Zhao Y, Zhao H, Wu W, Huang CX, Liu Y, Liu XY, Li HN, Li RKY. A review of microphase separation of polyurethane: Characterization and applications. *Polymer Testing*. 2022;107: 107489.

8. Zheng J, Ozisik R, Siegel RW. Disruption of self-assembly and altered mechanical behavior in polyurethane/zinc oxide nanocomposites. *Polymer*. 2005;46(24): 10873–10882.
9. Zheng J, Ozisik R, Siegel RW. Phase separation and mechanical responses of polyurethane nanocomposites. *Polymer*. 2006;47(22): 7786–7794.
10. Larraza I, Alonso-Lerma B, Gonzalez K, Gabilondo N, Perez-Jimenez R, Corcuera MA, Arbelaiz A, Eceiza A. Waterborne polyurethane and graphene/graphene oxide-based nanocomposites: Reinforcement and electrical conductivity. *Express Polymer Letters*. 2020;14(11): 1018–1033.
11. Kojio K, Kugumiya S, Uchiba Y, Nishino Y, Furukawa M. The microphase-separated structure of polyurethane bulk and thin films. *Polymer Journal*. 2009;41(2): 118–124.
12. Takahashi A, Kita R, Kaibara M. Effects of thermal annealing of segmented-polyurethane on surface properties, structure and antithrombogenicity. *Journal of Materials Science: Materials in Medicine*. 2002;13: 259–262.
13. Li X, Lu Y, Wang H, Pösel E, Eling B, Men Y. Crystallization of hard segments in MDI/BD-based polyurethanes deformed at elevated temperature and their dependence on the MDI/BD content. *European Polymer Journal*. 2017;97: 423–436.
14. Christenson EM, Anderson JM, Hiltner A, Baer E. Relationship between nanoscale deformation processes and elastic behavior of polyurethane elastomers. *Polymer*. 2005;46(25): 11744–11754.
15. Scetta G, Euchler E, Ju J, Selles N, Heuillet P, Ciccotti M, Creton C. Self-organization at the crack tip of fatigue-resistant thermoplastic polyurethane elastomers. *Macromolecules*. 2021;54(18): 8726–8737.
16. Shard AG, Davies MC, Tendler SJB, Jackson DE, Lan PN, Schacht E, Purbrick MD. Surface organization of polyurethanes observed by static secondary ion mass spectrometry. *Polymer*. 1995;36(4): 775–779.
17. McLean RS, Sauer BB. Tapping-mode AFM studies using phase detection for resolution of nanophases in segmented polyurethanes and other block copolymers. *Macromolecules*. 1997;30(26): 8314–8317.
18. Garrett JT, Siedlecki CA, Runt J. Microdomain Morphology of Poly(urethane urea) Multiblock Copolymers. *Macromolecules*. 2001;34(20): 7066–7070.
19. Alves P, Pinto S, de Sousa HC, Gil MH. Surface modification of a thermoplastic polyurethane by low-pressure plasma treatment to improve hydrophilicity. *Journal of Applied Polymer Science*. 2011;122(4): 2302–2308.
20. Chudinov V, Kondyurina I, Terpugov V, Kondyurin A. Weakened foreign body response to medical polyurethane treated by plasma immersion ion implantation. *Nuclear Instruments and Methods in Physics Research Section B: Beam Interactions with Materials and Atoms*. 2019;440: 163–174.
21. Morozov IA, Kamenetskikh AS, Beliaev AY, Izumov RI, Scherban MG, Lemkina LM, Kiselkov DM. Polyurethane treated in Ar/C₂H₂/Ar plasma: towards deformable coating with improved albumin adsorption. *Applied Sciences*. 2021;11: 9793.
22. Morozov IA, Kamenetskikh AS, Beliaev AY, Izumov RI, Bannikov MV, Scherban MG, Kiselkov DM. Carbon deposition and argon post-treatment of polyurethane surface: Structural-mechanical and fracture properties. *Surface and Coatings Technology*. 2022;437: 128372.
23. Santos TB, Vieira AA, Paula LO, Santos ED, Radi PA, Khouri S, Maciel HS, Pessoa RS, Vieira L. Flexible camphor diamond-like carbon coating on polyurethane to prevent *Candida albicans* biofilm growth. *Journal of the Mechanical Behavior of Biomedical Materials*. 2017;68: 239–246.
24. Barz J, Haupt M, Oehr C, Hirth T, Grimmer P. Stability and water wetting behavior of superhydrophobic polyurethane films created by hot embossing and plasma etching and coating. *Plasma Processes and Polymers*. 2019;16(6): 1800214.

25. Joshi M, Adak B, Butola BS. Polyurethane nanocomposite based gas barrier films, membranes and coatings: A review on synthesis, characterization and potential applications. *Progress in Materials Science*. 2018;97: 230–282.
26. Fronczak SG, Dong J, Browne CA, Krenek EC, Franses EI, Beaudoin SP, Corti DS. A new “quasi-dynamic” method for determining the Hamaker constant of solids using an atomic force microscope. *Langmuir*. 2017;33(3): 714–725.
27. Morozov IA. Atomic force microscopy nanoindentation kinetics and subsurface visualization of soft inhomogeneous polymer. *Microscopy Research and Technique*. 2021;84(21): 1959–1966.
28. Sneddon IN. The relation between load and penetration in the axisymmetric Boussinesq problem for a punch of arbitrary profile. *International Journal of Engineering Science*. 1965;3(1): 47–57.
29. Shulha H, Kovalev A, Myshkin N, Tsukruk VV. Some aspects of AFM nanomechanical probing of surface polymer films. *European Polymer Journal*. 2004;40(5): 949–956.
30. Garcia PD, Guerrero CR, Garcia R. Time-resolved nanomechanics of a single cell under the depolymerization of the cytoskeleton. *Nanoscale*. 2017;9(33): 12051–12059.
31. Guerrero CR, Garcia PD, Garcia R. Subsurface imaging of cell organelles by force microscopy. *ACS Nano*. 2019;13(8): 9629–9637.
32. Aishwarya S, Shanthi J, Swathi R. Surface energy calculation using Hamaker’s constant for polymer/silane hydrophobic thin films. *Materials Letters*. 2019;253: 409–411.
33. Stevenson MC, Beaudoin SP, Corti DS. Toward an improved method for determining the Hamaker constant of solid materials using atomic force microscopy. I. quasi-static analysis for arbitrary surface roughness. *J. Phys. Chem. C*. 2020;124(5): 3014–3027.

THE AUTHORS

Morozov I.A. 

e-mail: ilya.morozov@gmail.com

Beliaev A.Yu.

e-mail: belyaev@icmm.ru

Scherban M.G.

e-mail: ma-sher74@mail.ru